



A Hybrid Ice Hydrometeor Retrieval Algorithm for (Sub)millimeter-Wave Radiometers in Support of the PolSIR and PMM Missions

Yuli Liu^{1,2}, Jie Gong², Ian S. Adams², Rachael A. Kroodsma², Ruiyao Chen³, Dong L. Wu², Ralf Bennartz³, and Scott A. Braun²

¹Goddard Earth Sciences Technology and Research (GESTAR) II, University of Maryland Baltimore County (UMBC), Baltimore, MD 21250, USA

²NASA Goddard Space Flight Center, Greenbelt, MD 20771, USA

³Vanderbilt University, Nashville, TN 37240, USA

Correspondence: Yuli Liu (yuliliu@umbc.edu)

Abstract. This paper presents an ice hydrometeor retrieval algorithm for submillimeter-wave radiometers in support of the upcoming PolSIR (Polarized Submillimeter Ice Cloud Radiometer) and PMM (Precipitation Measuring Mission) satellite missions. The algorithm employs a hybrid Bayesian Monte Carlo Integration (BMCI) and Optimal Estimation Method (OEM) approach, which leverages the strengths of the BMCI method but extends the retrieval capability beyond the limitations of the a priori database when BMCI alone fails to identify enough database cases matching the observations. To address the highly non-Gaussian nature of the a priori statistics, a method using cumulative distribution functions (CDFs) and empirical orthogonal functions (EOFs) is applied to enable effective implementation of the OEM algorithm. With the CDFs/EOFs method, the OEM can maximize the posterior probability density function using the a priori constraint that is largely consistent with that used in the BMCI step, ensuring that the entire retrieval operates under a nearly uniform prior constraint.

The algorithm is first applied to evaluate the PMM-C²OMODO (Convective Core Observations through MicrOwave Derivatives in the trOpics) radiometer using simulated observations. Retrieval accuracies for key microphysical parameters are presented. Also, the retrieval diagnostics, including the vertical resolution, Degrees of Freedom (DoF), and Shannon information content, are analyzed. The algorithm is further applied to real CoSSIR (Configurable Scanning Submillimeter-wave Instrument/Radiometer) observations during the IMPACTS (Investigation of Microphysics and Precipitation for Atlantic Coast-Threatening Snowstorms) campaign, and the results are evaluated against the collocated triple-frequency radar retrievals from CRS (Cloud Radar System) and HIWARP (High-altitude Imaging Wind & Rain Airborne Profiler) observations. Multiple ice particle habits are examined, and both layer-resolved and column-integrated mass and size parameters are evaluated. Both simulated experiments and real-observation retrievals demonstrate that the hybrid BMCI-OEM method is highly effective in reducing simulated and observed brightness temperature (TB) discrepancies. With an appropriate selection of ice cloud particle habits, the TB simulations closely reproduce the observations. Using the logarithmic difference as the quantitative metric, the CoSSIR-retrieved ice water content, layer-resolved particle diameter, ice water path, and column-averaged mean mass diameter with the hybrid BMCI-OEM algorithm differ from triple-frequency radar retrievals by 3.75, 0.82, 2.53, and 0.55 dB,



respectively, representing reductions of 0.21, 0.02, 0.85, and 0.13 dB relative to BMCI-only retrievals. The hybrid Bayesian framework also demonstrates high extensibility to other remote-sensing observations. As more information becomes available through multi-sensor integration or the use of hyperspectral measurements, the hybrid Bayesian algorithm shows increasing potential to better constrain cloud microphysical properties.

1 Introduction

Submillimeter wavelengths comprise an important spectral regime for remotely sensing ice clouds properties (Buehler et al., 2007, 2012; Wu et al., 2024). Compared with traditional microwave frequencies, high-frequency radiometer channels have wavelengths comparable to ice particle dimensions, which makes them more responsive to ice particle scattering. Meanwhile, submillimeter waves have greater penetration depth through thick ice cloud compared with visible (VIS) or infrared (IR) bands. The submillimeter spectrum is therefore critical for bridging the gap in cloud and precipitation remote sensing. High-frequency radiometry for ice-cloud remote sensing has been validated through a series of field campaigns using airborne radiometers including CoSSIR (Compact Scanning Submillimeter Imaging Radiometer, later renamed the Configurable Scanning Submillimeter-wave Instrument/Radiometer, (Evans et al., 2005; Adams et al., 2020)) and ISMAR (International Submillimetre Airborne Radiometer, (Fox et al., 2017)) as well as several pathfinder spaceborne missions such as IceCube and the Arctic Weather Satellite (AWS). Notable suborbital campaigns include CRYSTAL-FACE (Cirrus Regional Study of Tropical Anvils and Cirrus Layers - Florida Area Cirrus Experiment, (Evans et al., 2005)), TC4 (Tropical Composition, Cloud and Climate Coupling, (Evans et al., 2012)), COSMICS (Cold-air Outbreak and sub-Millimetre Ice Cloud Study, (Brath et al., 2018)), and IMPACTS (Investigation of Microphysics and Precipitation for Atlantic Coast-Threatening Snowstorms, (McMurdie et al., 2022; Yorks et al., 2025)). Launched in 2016, IceCube was the first experimental spaceborne submillimeter radiometer operating at 883 GHz. IceCube has demonstrated its anticipated scientific value by capturing a wide dynamic range of ice water path (IWP) and showing sensitivity to ice particle size, while also validating the space technology readiness for submillimeter radiometers (Gong et al., 2021). In August 2024, the European Space Agency (ESA) launched the pathfinder operational satellite AWS into polar orbit, and it has been continuously collecting high-quality data ever since (Eriksson et al., 2025). In the coming years, several satellite missions equipped with high-frequency radiometers are expected to launch. Key missions include ESA's ICI (Ice Cloud Imager, (Eriksson et al., 2020)), NASA's PolSIR (Polarized Submillimeter Ice-cloud Radiometer), and the C²OMODO (Convective Core Observations through MicrOwave Derivatives in the trOpics, (Brogniez et al., 2022; Auguste and Chaboureau, 2022)) planned for the JAXA (Japan Aerospace Exploration Agency) and NASA PMM (Precipitation Measuring Mission, (Iki et al., 2025)). These missions represent major steps toward achieving global ice cloud observations from space.

The retrieval algorithms applied in high-frequency microwave ice cloud studies are fundamentally based on Bayes' theorem, which specifies knowledge in terms of probability density function (PDF) and combines prior information with observations to constrain the state variables. Among various algorithmic approaches, the Bayesian Monte Carlo Integration (BMCI) (Evans et al., 2002, 2005) and Quantile Regression Neural Network (QRNN) (Brath et al., 2018; Pfreundschuh et al., 2018; May



et al., 2024; May and Eriksson, 2025) are two representative implementations of the Bayesian framework. Both algorithms depend on a precalculated retrieval database, which consists of random atmospheric and cloud samples distributed according to the a priori PDF and the corresponding simulated brightness temperatures (TBs). The BMCI method assigns weights to the random samples based on the likelihood functions and integrates over the posterior PDF to obtain the mean state and the standard deviation. The QRNN approach uses the a priori database as a training dataset to learn the statistical distribution to predict state variables for new observations. Both algorithms have been thoroughly evaluated using simulated and real airborne observations, and they are planned to be operationally implemented in the upcoming ICI mission (Eriksson et al., 2020; May et al., 2024).

The primary limitation of these database-driven methods is the sparse coverage of the measurement space by database cases. Theoretically, both BMCI and QRNN require adequate database samplings that match the input TBs within the measurement uncertainty. In practice, however, even a large retrieval database inevitably has regimes in the multidimensional measurement space that are sparsely populated, especially when the dimensionality of the measurement vector is high or the measurement uncertainty is small. A common strategy to mitigate this issue is to expand the size and coverage of the retrieval database. Although this approach increases the likelihood of finding cases similar to the observations, the inherent measurement sparsity issue cannot be fully eliminated, as a precalculated database cannot cover all possible conditions. The quality and representativeness of the database constrain the maximum achievable performance for database-driven approaches.

Within the Bayesian framework, the Optimal Estimation Method (OEM) provides a rigorous approach to estimate state variables under prior constraints. Rodgers (2000) established a comprehensive theoretical foundation for the OEM method, and the method has since been widely applied in many atmospheric remote sensing applications (Austin et al., 2009; Pfreundschuh et al., 2020; Liu and Adams, 2025). Nevertheless, its application to submillimeter-wave radiometry for ice cloud retrievals presents several fundamental challenges. First, OEM assumes a Gaussian a priori PDF, but the actual distributions of atmospheric and cloud variables are typically strongly non-Gaussian. Second, OEM assumes a moderately nonlinear forward model, which makes selection of the initial state of iteration important. Third, as the radiative transfer model involves multiple scattering calculations in clouds, no analytical method exists for the rapid computation of the Jacobian matrix.

To leverage the strengths of the database-driven method while retaining the ability to exceed the limitations of the database when BMCI-alone fails, we adopt the hybrid BMCI and OEM strategy proposed by Evans et al. (2012) and extend the method to a state-of-the-art radiative transfer model. We present a detailed description of the retrieval algorithm and assess it using simulated observations as well as real observations collected during the IMPACTS field campaign. The paper is structured as follows. Section 2 provides a detailed description of the hybrid BMCI and OEM algorithm. Section 3 applies the hybrid algorithm to the evaluation of the C²OMODO sensor using simulated observations. Section 4 presents retrieval examples using real CoSSIR observations collected during the IMPACTS campaign and their validation against collocated triple-frequency radar measurements. Finally, Section 5 summarizes the results and discusses the strengths and limitations of the retrieval algorithm, as well as possible directions for future improvements.



2 Hybrid BMCI-OEM retrieval algorithm

90 2.1 Algorithm overview

The hybrid BMCI-OEM algorithm leverages the strengths of the BMCI method and overcomes the limitations imposed by the TB sparsity of the a priori database. With a high-quality retrieval database, BMCI is expected to serve as the primary method for producing retrievals under most conditions. When BMCI fails due to an insufficient number of database cases matching the input TB observations, OEM is applied to maximize the posterior PDF and extend the retrieval capability beyond
95 the constraints of the a priori database. Several techniques are employed to address the OEM implementation challenges. As a result, the OEM step can minimize the TB discrepancy using prior information that is largely identical to that used in the BMCI step.

Several key steps in the OEM implementation are worth noting. First, the CDF (Cumulative Distribution Function) and EOF (Empirical Orthogonal Function) technique proposed by Evans et al. (2012) is employed to address the OEM's requirement
100 for a Gaussian a priori PDF. The CDFs capture the complete single-point statistical information of the a priori data, and the EOFs capture the second-order statistics characterized by the correlation matrix. Using this approach, the highly non-Gaussian a priori PDF can be transformed into a multivariate Gaussian distribution in the eigen space. Second, OEM is initialized with the BMCI estimates, which are typically close to the final optimal state. This relaxes the moderate linearity requirement of the forward model and reduces the number of iterations needed. Third, since the radiative transfer model does not have an
105 analytical format for quick Jacobian matrix computation, we use the finite difference method by perturbing the state vector in the eigen space and computing the corresponding TB sensitivities.

2.2 Retrieval database

The retrieval database is a critical component of the hybrid BMCI-OEM algorithm. By establishing a comprehensive retrieval database, the computationally efficient BMCI method can handle most retrieval cases and produce reliable retrievals on its own.
110 A high-quality retrieval database requires that the atmospheric and cloud samples be distributed according to prior knowledge and that the corresponding simulated TB observations densely cover the possible regimes of the measurement space.

2.2.1 A priori profiles

To support the PolSIR and PMM missions, we build a comprehensive retrieval database using CloudSat and CALIPSO (Cloud-Aerosol Lidar and Infrared Pathfinder Satellite Observation) products. Compared with cloud resolving models that rely on
115 simplified and uncertain microphysical parameterizations (Kummerow et al., 2011), CloudSat-CALIPSO products are directly constrained by complementary active measurements and therefore provide a more observation-grounded and globally consistent representation of cloud microphysical structure across a wide range of cloud regimes. At the current stage of development, a balance between the database size and computational cost is achieved by selecting one orbit every three days from the full year of 2007 within the tropical region (30°S–30°N). Approximately 1.5 million all-sky atmospheric and cloud profiles are



120 selected. The ice water content (IWC) profiles are obtained from the 2C-ICE product, which is retrieved using synergistic
CloudSat and CALIPSO observations and covers a large dynamic range from thin to dense ice cloud layers (Deng et al., 2015).
With a W-band Cloud Profiling Radar, CloudSat experiences significant attenuation in thick clouds such that extremely large
IWP cases are likely underrepresented in the a priori database. The liquid water content (LWC) profiles are obtained from the
2B-CWC-RO product, and the thermodynamic profiles and surface parameters are provided by the auxiliary ECMWF dataset.
125 The vertical resolution of the atmospheric and cloud profiles is set to 240 meters.

2.2.2 Radiative transfer model

We develop the radiative transfer model (RTM) using ARTS (Buehler et al., 2018), which is widely recognized as one of the
most rigorous RTMs in representing multiple scattering within clouds. The developed forward model includes one ice hydrometeor
type and one liquid hydrometeor type. The scattering properties of each hydrometeor type are determined by its single
130 scattering data (SSD) and particle size distribution (PSD). For ice clouds, due to the diversity of particle shapes in nature and
the significant variations in their scattering properties, we select five representative particle shapes to approximate the natural
conditions. The chosen particle shapes (designated by LargePlateAggregate, LargeBlockAggregate, LargeColumnAggregate,
6BulletRosette, and EvansSnowAggregate) align with the selection in May et al. (2024). Liquid cloud particles are assumed to
be spherical. All particles are assumed to be randomly oriented, and their SSDs are obtained from the ARTS scattering dataset
135 (Eriksson et al., 2018). A one-moment PSD scheme is assumed for both ice and liquid clouds. The PSD scheme proposed by
Field et al. (2007) for a tropical regime is applied to cloud ice, and the modified gamma distribution scheme is used for cloud
liquid. The absorbing gases include O₂, N₂, O₃, and water vapor. The surface emissivity over ocean and land is calculated
using the TESSEM (Tool to Estimate Sea-Surface Emissivity from Microwave to Submillimeter Waves, (Prigent et al., 2017))
and the TELSEM (Tool to Estimate Land-Surface Emissivities at Microwave frequencies, (Aires et al., 2011)), respectively.
140 The DISORT (DIScrete-Ordinate-method Radiative Transfer, (Stamnes et al., 1988)) scattering solver is employed, and the
simulations are currently limited to the first Stokes parameter. A pencil-beam is assumed in computing the TB simulations, and
instrument parameters will be integrated later when the sensors are finalized.

The ice cloud particle size is computed as part of the radiative transfer calculations. Since both ice and liquid hydrometeor
PSD schemes are one-moment, the IWC and LWC values from the 2C-ICE and 2B-CWC-RO products can be directly mapped
145 to particle size parameters at each vertical layer. At each layer, the characteristic particle size D_{me} is defined as the mass-
weighted mean of the volume equivalent diameter D_{veq} :

$$D_{me} = \frac{\sum N(D_{veq}) * D_{veq}^4}{\sum N(D_{veq}) * D_{veq}^3} \quad (1)$$

where D_{veq} is provided by the ARTS SSD dataset, and $N(D_{veq})$ is the number concentration in each particle size interval
computed by the ARTS PSD scheme. Subsequently, the column-averaged mean mass diameter D_m for each ice and liquid
150 hydrometeor profile is computed as the IWC- or LWC-weighted mean of D_{me} .



2.3 BMCI algorithm

Using the precalculated retrieval database, the hybrid BMCI-OEM algorithm first performs the BMCI retrieval. Since the database samples are already distributed according to the a priori PDF, the posterior PDF is determined by the likelihood function, which quantifies how well the database TB simulations match the observations relative to the measurement uncertainties:

155

$$P_{post}(x|y_{obs}) \propto \exp\left(-\frac{1}{2}\chi_y^2\right) \quad \chi_y^2 = \sum_{j=1}^N \frac{(y_{sim,j} - y_{obs,j})^2}{\sigma_j^2} \quad (2)$$

where $y_{sim,j}$ and $y_{obs,j}$ are the simulated and observed TB in the j th channel, σ_j is the measurement noise characterized by the noise equivalent differential temperature (NEDT), and N is the number of radiometer channels. The retrieval result and associated uncertainty are derived by integrating over the posterior PDF to find the mean state and standard deviation:

$$x_{ret} = \sum_i x_i * p_{post}(x_i|y_{obs}) \quad \sigma_x^2 = \sum_i (x_i - x_{ret})^2 * p_{post}(x_i|y_{obs}) \quad (3)$$

The BMCI algorithm does not require the prior PDF to follow a specific functional form. It is also computationally efficient as no additional radiative transfer calculations are needed. However, its primary limitation is the database sparsity in the measurement space. The successful implementation of the BMCI requires that a minimum number of database cases (25 in this study, consistent with Evans et al., 2005) fall within a specified χ_y^2 threshold. Due to the finite size of the prior database, this requirement cannot always be satisfied, particularly when the number of sensor channels is large or the measurement noise for each channel is small. In such cases, the BMCI algorithm theoretically fails. One method to obtain reliable retrievals and uncertainty estimates is to inflate the measurement uncertainty NEDT until the specified number of database cases is reached, after which the posterior PDF is integrated, as shown in Eq. (3). This approach sacrifices the measurement accuracy and is therefore not optimal. Alternatively, as developed in this study, the OEM optimization procedure is implemented to further maximize the posterior PDF.

170

2.4 OEM Algorithm

One major challenge in implementing the OEM algorithm is that the OEM requires the a priori PDF to be Gaussian, but the distribution of cloud variables in the retrieval database is highly non-Gaussian. To address the mismatch, we apply the CDF/EOF technique developed by Evans et al. (2012) to capture the statistical characteristics of the retrieval database and transform the a priori information into the eigen space. The core idea of the CDF method is to map the rank of a state variable at a given layer in the retrieval database to the CDF of the standard normal distribution. Through the rank-based mapping, the atmospheric variables and their Gaussian representations can be mutually transformed. For the retrieval database, the CDFs of the state variables including IWC, LWC, and water vapor at each layer are computed by sorting the parameter values and assigning ranks. To avoid discontinuities in ranking, layers identified as clear are replaced with small random values below the instrument sensitivity threshold. The hydrometeor parameters are represented by their ranking. At each layer, these ranked values are mapped onto the CDF of a standard normal distribution to convert them into Gaussian-distributed points. The

180



CDF mapping process is applied layer by layer to the profiles of IWC, LWC, and water vapor, and the database samples are transformed into Gaussian space. The covariance matrix S_{ga} between different layers and variables of the Gaussian-distributed points is computed.

185 The EOF method is further applied to capture the correlations between variables at different levels and reduce the state vector dimensionality and computational cost. The eigenvalues and eigenvectors of the covariance matrix S_{ga} are computed. The eigenvectors define a new set of orthogonal coordinates, with the variability of the data along each coordinate characterized by the corresponding eigenvalue. By defining the OEM state vector in eigen space, the cost function to be minimized in the OEM is given by:

$$190 \quad J = \sum_{i=1}^{N_{dim}} \xi_i^2 + \sum_{j=1}^{N_{chan}} \frac{(y_{obs,j} - F_j[G(\xi)])^2}{\sigma_j^2} \quad (4)$$

where ξ is the state vector, $G(x)$ denotes the function mapping the state vector from the eigen space back to the corresponding atmospheric and cloud variables, and $F(x)$ represents the forward model simulations. The eigenspace state vector ξ consists of the corresponding eigenspace representations of the original IWC, LWC, and water vapor profiles. ξ is first transformed back to Gaussian space ξ_g by scaling each EOF component by the square root of the eigenvalue and then multiplying by the corresponding eigenvectors to rotate back to the original coordinate system. The vector ξ_g is then converted back to atmospheric and cloud profiles. For each ξ_g element, its standard normal CDF value is computed and mapped back to the corresponding geophysical parameters by interpolating the relationship between CDF values and cloud parameters at the same layer in the a priori database. This procedure is applied sequentially to all elements of the Gaussian state vector ξ_g .

The OEM iteration starts with the BMCI-estimated results. When an insufficient number of database cases is found, we 200 inflate the measurement uncertainty NEDT in a step of $\sqrt{2}$ until reaching the required number of database cases (Evans et al., 2005; Liu et al., 2018), after which the mean state estimate is computed. The state vector in the eigen space corresponding to the BMCI estimate is computed and used as the initial guess for the OEM iteration. As no analytical method is currently available for computing Jacobians that include multiple-scattering effects in ARTS, the Jacobian matrix is computed numerically by perturbing each state element in eigen space and computing the corresponding TB sensitivities. With the Jacobian matrix, the 205 robust Levenberg-Marquardt (LM) method is employed to iteratively update the state vector. The iteration stops when reaching a stable state, and the associated uncertainty estimate is computed as:

$$S_p = (S_a^{-1} + K S_y^{-1} K)^{-1} \quad (5)$$

where S_a is the a priori covariance matrix of the state vector ξ , S_y is the covariance matrix of measurement error, and K is the Jacobian matrix of $F(G(\xi))$. Other retrieval diagnostics such as the averaging kernel matrix are produced as well.

210 Since Eq. (5) provides uncertainty estimates of the state vector in eigen space rather than for the geophysical variables of interest, we apply a Cholesky decomposition of the posterior covariance matrix to generate an ensemble of random cases around the converged state in eigen space (Evans et al., 2012). The ensemble members are then transformed back to atmospheric and cloud variables, and MCI is performed to compute the uncertainty estimates for the variables of interest, including vertical



215 profiles of ice and liquid cloud microphysics and water vapor, as well as the corresponding column-integrated quantities such as IWP, D_m , liquid water path (LWP), and integrated water vapor (IWV).

3 Simulation experiment

3.1 Retrieval accuracy

In this section, we apply the hybrid BMCI-OEM algorithm to assess the performance of the C²OMODO sensor in the PMM missions using simulated observations. C²OMODO is a satellite mission supported by the French space agency Centre National D'Études Spatiales as a contribution to the JAXA-NASA PMM mission. C²OMODO includes one window channel at 89 GHz, 220 five channels at the 183.31 GHz absorption line, and four channels at the high-frequency 325.15 GHz absorption line. The detailed channel frequencies and corresponding measurement uncertainties NEDT are summarized in Table 1. It should be noted that the listed NEDT characterizations are used only to evaluate the algorithm performance. The true values remain undetermined.

Table 1. Channel characteristics assumption of the C²OMODO radiometer. The NEDT values correspond to those used in the simulation experiment. The actual values remain undetermined.

Frequency (GHz)	NEDT(K)	Frequency (GHz)	NEDT(K)
89	0.5	325.15±10.7	1.5
183.31-10.7	0.75	325.15±7.0	1.5
183.31-7.0	0.75	325.15±4.9	1.5
183.31-4.9	0.75	325.15±3.05	1.5
183.31-3.05	0.75	325.15±0.8	1.5

225 In the simulation experiment, independent cloud profiles for testing are obtained in the same way as the a priori database but using CloudSat products from a different year. From the full year of 2008 CloudSat data, atmospheric and cloud profiles from one orbit every three days are first extracted, following the same procedure as for the a priori database. From these, 30,000 all-sky atmospheric and cloud cases are randomly selected, approximately half of which contain at least one ice cloud layer. The same radiative transfer model used to construct the retrieval database is employed to compute the simulated TB observations. 230 After adding Gaussian noise with a standard deviation set according to the assumed NEDT, the simulated observations are input into the hybrid retrieval algorithm, and the retrieved results are compared with the reference values for evaluation. This simulation experiment uses an idealized configuration in which the identical forward model with the same particle habit selection is applied for both simulating the observations and performing the retrievals. The figures presented in this section are based on the LargeBlockAggregate particle habit assumption by default unless noted otherwise. We have also evaluated the 235 impact of inconsistent microphysics assumptions between the a priori database and the retrievals. However, this is not the focus of the current study and therefore the results are not included. All results presented here assume nadir-only observations: we



acknowledge that both the PolSIR and PMM-C²OMODO radiometers are cross-track scanners, and results at off-nadir angles can be slightly different.

Figure 1 presents the retrieval results for the C²OMODO radiometer in the idealized simulation experiment based on the hybrid BMCI-OEM algorithm. The top panels show the retrieval results for IWP, LWP, IWV, and D_m compared with the reference, and the bottom panels display the associated retrieval uncertainties. The C²OMODO sensor channel set demonstrates good retrieval capability for IWP. Since no inconsistencies in particle habit or PSD selections in the forward model are included in this idealized experiment setting, the median retrievals follow the diagonal line until IWP falls below approximately 30 $g m^{-2}$, where the retrieved values start to exhibit systematic negative biases for thin ice clouds. The black dotted lines indicate the $\pm 100\%$ accuracy bounds that are defined as the range between $0.5 \cdot IWP_{true}$ and $2 \cdot IWP_{true}$ for reference. At high IWP values, the scatter points closely follow the diagonal with minimal spread, and the dispersion increases as IWP decreases. For retrieval uncertainties, when IWP exceeds approximately 100 $g m^{-2}$, most uncertainty estimates fall within the 100% range. For smaller IWP values, the uncertainty estimates increase rapidly. Since C²OMODO has an 89 GHz channel that is sensitive to both ice scattering and liquid emission, the sensor demonstrates some capability for retrieving liquid cloud total mass when LWP is beyond 100 $g m^{-2}$. The retrieved LWP values generally exhibit a small negative bias, and the associated retrieval uncertainties remain high. This is expected due to the absence of low-frequency channels that are primarily sensitive to liquid hydrometeor emissions. The C²OMODO sensor also demonstrates the capability of constraining water vapor as both 183 GHz and 325 GHz channels are centered on water vapor absorption lines. The retrieved IWV values closely follow the true values with little scatter throughout the entire dynamic range, and the uncertainty estimates are generally below 5 $kg m^{-2}$. For the ice cloud particle size, when the true D_m exceeds roughly 400 μm , the median retrieval closely follows the diagonal. For D_m below 400 μm , the retrieved values tend to underestimate the truth. The corresponding uncertainty estimates remain mostly below 100 μm for D_m larger than 400 μm , and they increase substantially for smaller ice particles.

Figure 2 compares the BMCI-only and hybrid BMCI-OEM retrievals to investigate the benefits of the additional OEM procedure. When the BMCI fails to find enough database matches, the BMCI-only results are obtained by inflating the NEDT in a step of $\sqrt{2}$ until the required number of cases is reached. Approximately 7% of the all-sky testing samples require the NEDT inflation step, and these are the same set of samples for which the OEM procedure is applied. The left panel compares the χ_y^2 values for the BMCI-only and the OEM retrievals. As the OEM iteration is initialized with the BMCI estimate, the comparison also illustrates how the χ_y^2 values change before and after applying the OEM step. The figure shows a substantial reduction in χ_y^2 after applying the OEM. For the BMCI-only results, many χ_y^2 values exceed 10^2 , and some exceed 10^3 . After the OEM step, the χ_y^2 decreases significantly, with most values falling below 10^1 and are within the range expected from the measurement uncertainty. One more point to note is that the BMCI-only failures occur over a wide range of IWP values. The middle and right panels compare the retrieval results in terms of IWP and D_m in this idealized OSSE. The results indicate that the OEM step provides moderate but consistent improvements in accuracy relative to the BMCI-only retrievals. The improvements are particularly evident for IWP values greater than 1 $kg m^{-2}$ and for large particle sizes. It should be noted that the BMCI retrieves the column-integrated IWP and D_m directly, whereas the OEM first retrieves the vertical profiles and then

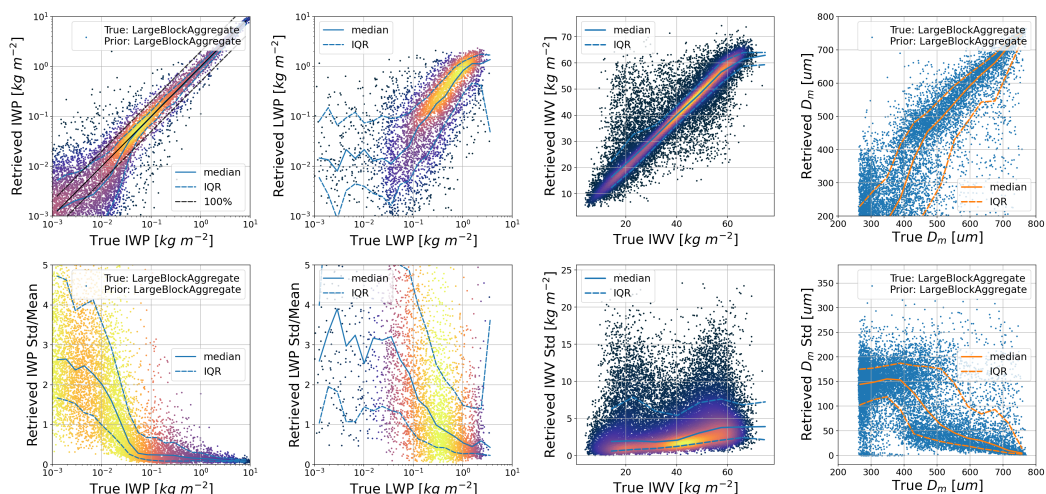


Figure 1. Retrieval results for the C²OMODO radiometer in an idealized simulation experiment using the hybrid Bayesian Monte Carlo Integration (BMCI) and Optimal Estimation Method (OEM) retrieval algorithm. The top panels compare the retrieved ice water path (IWP), liquid water path (LWP), integrated water vapor (IWV), and mean mass diameter (D_m) with the true values, and the bottom panels show the corresponding retrieval uncertainties.

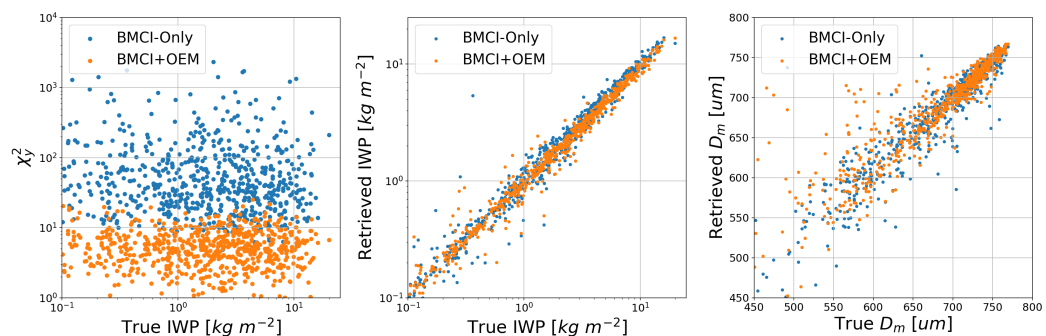


Figure 2. Comparison of the BMCI-only and hybrid BMCI-OEM retrievals in an idealized simulation experiment, with the left panel showing the χ_y^2 values that quantify the mismatch between the simulated and observed brightness temperature, the middle panel showing the retrieval accuracy for IWP, and the right panel showing the retrieval accuracy for the mean mass diameter D_m .

performs the vertical integration. Since these two retrieval results are not necessarily equivalent, the improvements achieved through the OEM step become particularly noteworthy.

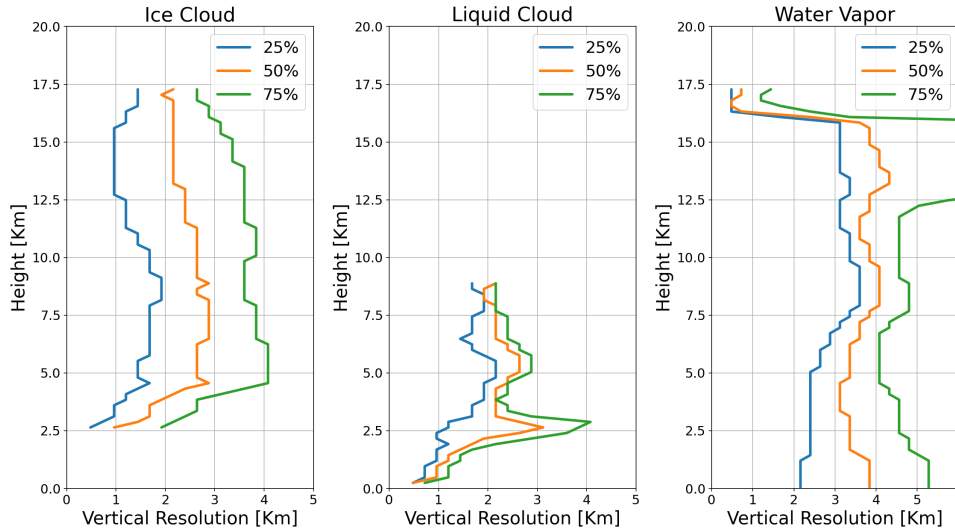


Figure 3. The median and interquartile-range (IQR) profiles of the vertical resolution for the ice hydrometeor, liquid hydrometeor, and water vapor, as derived from the averaging kernel matrix in an idealized simulation experiment.

3.2 Retrieval diagnostics

The OEM framework also provides diagnostic parameters for assessing the quality and reliability of the retrieval results. In this study, we focus on three key diagnostics: vertical resolution, degrees of freedom (DoF), and Shannon information content. To make a more comprehensive analysis, even in cases where BMCI alone can perform the retrieval, a single OEM iteration is still executed to compute the Jacobian matrix and associated diagnostic quantities. For the cases in which OEM is applied, the final Jacobian matrix and associated diagnostic quantities are used in this evaluation.

To assess the vertical resolution, the averaging kernel matrix is first calculated:

$$A = (S_a^{-1} + K S_y^{-1} K)^{-1} S_a^{-1} \quad (6)$$

The vertical resolution at each level is then computed as the full width at half maximum (FWHM) of the corresponding row of the averaging kernel matrix. By separating the elements of the Jacobian matrix into ice cloud, liquid cloud, and water vapor, the averaging kernel matrix and the vertical resolution are computed for different types separately. Figure 3 shows the median and interquartile-range (IQR) profiles of the vertical resolution for ice, liquid, and water vapor. The median vertical resolution of ice clouds is seen to range between 2 and 3 km, with the IQR spanning 1 to 4 km. The resolution is typically smaller at the cloud top than at the bottom, with a median of about 2 km near the top and around 2.7 km below 11 km. The results are highly consistent with those in May et al., 2025. The C²OMODO channel set also shows sensitivity to liquid clouds, with a median vertical resolution also in the 2-3 km range. For water vapor, the median resolution is approximately 4km under all-sky atmospheric conditions.

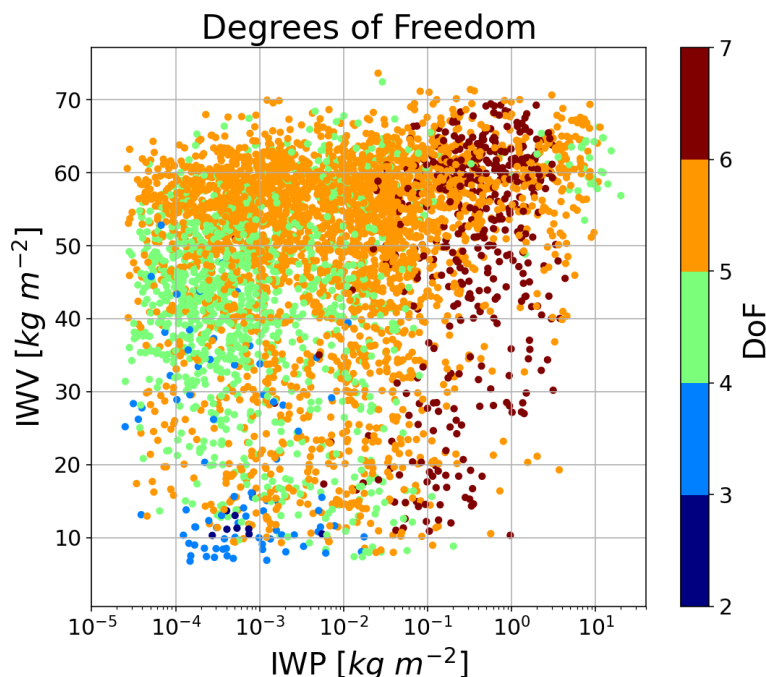


Figure 4. The scatter plot of the Degrees of Freedom (DoF) as a function of ice water path (IWP) and integrated water vapor (IWV) that are derived from an idealized simulation experiment.

290 From the averaging kernel matrix, the DoF is computed to quantify the effective number of independent pieces of information provided by the observations. The DoF is computed as the trace of the averaging kernel matrix in Eq. (6). Figure 4 shows the scatter plot of the DoF as a function of IWP and IWV. The DoF generally increases with both IWP and IWV. When the ice cloud is absent or very thin ($IWP < 10^{-2} \text{ kg m}^{-2}$), $DoF < 4$ typically occurs in conditions that are dry ($IWV < 40 \text{ kg m}^{-2}$). DoF values between 4 and 5 are more common when IWV ranges from 40 and 55 kg m^{-2} , while $DoF > 5$ are frequent when

295 IWV exceeds 55 kg m^{-2} . These low IWP values corresponds to the “clear-sky” retrieval capability for the water vapor profile. Specifically, using the assumed C²OMODO channel set, 4-6 DoFs for water vapor can be independently retrieved, consistent with the overall SAPHIR (Sondeur Atmosphérique du Profil d’Humidité Intertropicale par Radiométrie) water vapor retrieval capability on which the C²OMODO instrument is based (Mathur et al., 2013). The DoF is mostly 5-6 when a relatively thin ice cloud is present ($10^{-2} \text{ kg m}^{-2} < IWP < 10^{-1} \text{ kg m}^{-2}$) and increases to 6-7 for thicker ice clouds where the sensor

300 frequencies are particularly sensitive (IWP between $2 \cdot 10^{-1} \text{ kg m}^{-2}$ and 3 kg m^{-2}). The larger DoF observed when an ice cloud is substantial corresponds to the sensor’s ability to retrieve information about the vertical distribution of ice cloud mass and particle size, while the capability to resolve the vertical distribution of water vapor is lost, as indicated by the flattening of the gradient on the ordinate. The DoF decreases to about 4-5 at the highest IWP values, indicating information saturation when the ice cloud becomes too thick.



305 The Shannon information content measures the reduction of uncertainty in the retrieved state compared to the prior PDF and
quantifies how much information the observations contribute beyond the prior knowledge. The Shannon information content
is computed as:

$$H = \frac{1}{2} \log_2 |S_a S_p^{-1}| \quad (7)$$

where S_a and S_p denote the a priori and posterior PDFs of the state vector, respectively. The value H is expressed in bits, where
310 n bits indicate that the measurements reduce the state uncertainty by a factor of 2^n . As the information from different channels
is partially redundant, the sum of per-channel information is not equal to the total information content when all channels are
combined. To quantify the contribution of each channel, we compute the incremental information content by starting with a
single channel and adding channels one at a time until all channels are included. The sequence begins with the 183.31-10.7 GHz
channel, followed by the remaining 183 GHz channels, then the 325 GHz channels, and finally the 89 GHz channel. Figure 5
315 presents the incremental Shannon information content for IWP, LWP, and IWV, respectively. For IWP, the information content
generally increases with increasing IWP but lowers at the high end. Starting from around 20 g m^{-2} , the information content
rises at an approximately constant rate up to about 1 kg m^{-2} , beyond which the rate of growth slows. The combined 183
GHz channels provide approximately 5 bits of information at an IWP of 100 g m^{-2} and reach a maximum of about 10 bits at
an IWP of approximately 3 kg m^{-2} . Adding a single 325 GHz wing band ($325 \pm 10.7 \text{ GHz}$) provides approximately 1 bit of
320 information even when IWP is extremely small, and the five 325 GHz channels contributes roughly 4 bits of information for
higher IWP. The addition of channel 9 ($325 \pm 0.8 \text{ GHz}$) produces the largest incremental increase in information content among
the 325 GHz channels. This result suggests that a channel closer to the water vapor absorption line at 325 GHz may better
sense cloud-top information or more effectively distinguish between cloud and water vapor signals near the cloud top. The 89
GHz channel contributes noticeably only at the high end of the IWP range, probably because of its unique role in separating
325 liquid from ice hydrometeors as precipitation often occurs in this IWP range.

For LWP, channels 1 to 3 show some sensitivity to liquid cloud, but channels 4 to 9 contribute very little information due to
strong attenuation by water vapor and overlying ice clouds. The 89 GHz channel produces the largest increase in information
content for liquid clouds. For IWV, the 183 GHz channels exhibit clear sensitivity, with each additional subchannel producing
a noticeable increase in information content across the entire IWV range. Among the 325 GHz channels, only channel 9, which
330 is closest to the water vapor absorption line, exhibits evident sensitivity, while the other channels contribute very little. The
89 GHz channel is situated in an atmospheric window but is influenced by the water-vapor continuum, and it is observed to
provide substantial information for IWV. This Shannon information content analysis demonstrates not only the scientific merit
of the new 325 GHz submillimeter bands but also highlights the importance of including traditional high-frequency channels
(89 and 183 GHz) to achieve high-quality all-sky retrievals of ice and liquid hydrometeors as well as water vapor.

335 4 Field campaign retrieval validation

In this section, we apply the hybrid BMCI-OEM algorithm to real observations collected during the IMPACTS field cam-
paign to further evaluate the retrieval performance. IMPACTS is a NASA-sponsored field campaign to study wintertime

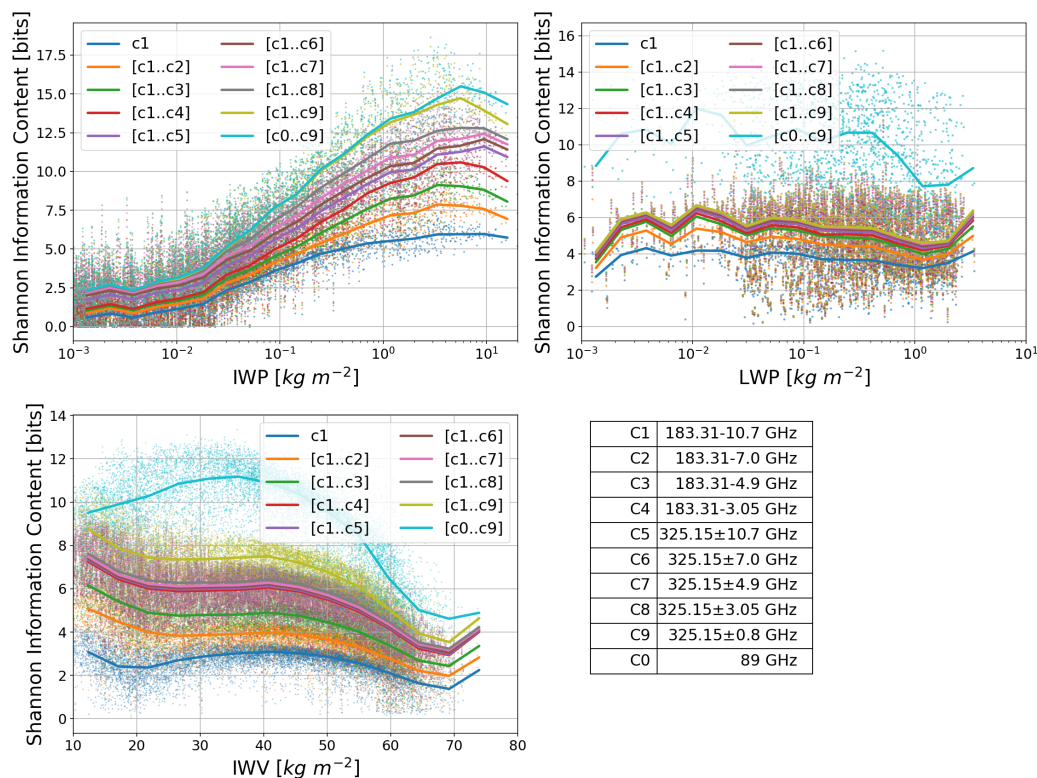


Figure 5. The Shannon information content of C²OMODO radiometer for ice water path (IWP), liquid water path (LWP), and integrated water vapor (IWV). The incremental information content is computed by starting with a single channel and adding channels one at a time until all channels are included. The sequence begins with the 183.31-10.7 GHz channel, followed by the remaining 183 GHz channels, then the 325 GHz channels, and finally the 89 GHz channel.

snowstorms associated with East Coast cyclones. The campaign flew a complementary suite of remote sensing and in-situ instruments during the boreal winters of 2020-2023 to collect measurements essential for snow process studies. CoSSIR has
 340 been upgraded with new front-end receivers, configurable scanning patterns, and dual-polarization capability across all channels, thereby increasing its flexibility for simulating a variety of spaceborne submillimeter radiometers, including PolSIR and PMM-C²OMODO. The newly upgraded CoSSIR was first deployed aboard the ER-2 aircraft during the final phase of the IMPACTS campaign in the 2022-2023 winter and operated in a hybrid conical and along-track scanning mode. This was also
 345 the first time CoSSIR flew over mid- and high-latitude winter weather conditions. The CoSSIR instrument includes four sub-channels near 183 GHz, four subchannels near 325 GHz, and one channel at 684 GHz, all of which are dual-polarized. The detailed characteristics of channel frequency and NEDT are listed in Table 2. On the same ER2 aircraft platform, the W-band CRS (Cloud Radar System, (McLinden et al., 2021)) and the dual-frequency Ka/Ku-band HIWRAP (High-altitude Imaging Wind & Rain Airborne Profiler, (Li et al., 2015)) radars were also deployed. The collocated triple-frequency radar observations



provide detailed cloud structure and a reliable reference for validating the hybrid BMCI-OEM algorithm's performance from
350 CoSSIR observations.

Table 2. Channel characteristics of the CoSSIR radiometer during the IMPACTS field campaign.

Frequency (GHz)	NEDT(K)	Frequency (GHz)	NEDT(K)
170.5	0.2	325.15±11.5	1.5
177.31	0.2	325.15±3.4	1.5
180.31	0.2	325.15±0.9	1.5
182.31	0.2	684.0	1.0

4.1 CoSSIR retrieval settings

A major difference from the retrieval implementation in Section 3 is the update of the a priori database. Since the retrieval database prepared for PolSIR and PMM-C²OMODO in Section 2.2 is specific to the tropical region, we develop a separate a priori database for the IMPACTS field campaign. The construction of the new database follows the same procedure described
355 in Section 2.2, but it uses different subsets of CloudSat products. All CloudSat datasets from winter 2005-2019 are examined, and profiles with IWP greater than 10 g m^{-2} are selected when they fall within a selected latitude-longitude box over the East Coast of the United States that covers the IMPACTS region. The same radiative transfer model and same selection of the ice cloud particle habits described in Section 2.2.2 are applied. With this new a priori database, the hybrid BMCI and OEM algorithm is applied to the real CoSSIR observations to produce retrieval results. Only the nadir TB observations are used to
360 enable a direct comparison with retrievals from the collocated triple-frequency radar observations, with the latter serving as the reference. The atmospheric profiles and surface parameters required for the radiative transfer calculations are obtained from the Weather Research and Forecasting (WRF) model outputs supporting the IMPACTS field campaign.

4.2 Triple-frequency radar retrieval settings

One advantage of the hybrid BMCI-OEM algorithm is its great extendibility to other types of remote sensing observations. By
365 updating the forward model to include a radar simulator and replacing the TB observations with radar reflectivity profiles in the measurement vector, the hybrid BMCI-OEM algorithm is directly adapted for triple-frequency radar retrievals. The same ARTS forward model used for TB simulations is upgraded to include the ARTS built-in single-scattering radar solver for simulating radar reflectivities at different bands.

The triple-frequency radar observation profiles are interpolated to the same 240-meter vertical resolution as the a priori
370 database. Since only ice clouds are of interest in this study, we only focus on layers where at least one of the triple-frequency radar reflectivities exceeds its minimum detection limitation and the temperature, according to the WRF temperature profile, is below 273 K. The range bins below the melting layer are excluded. The state vector is defined as the IWC in these layers, and the measurement vector consists of the triple-frequency radar observations in these layers that are above their respective



detection thresholds. To obtain the initial profile for the OEM iteration, we build a pre-calculated database containing random
375 IWC samples and their corresponding triple-frequency radar reflectivity simulations. In each layer, the IWC is determined by
selecting the database sample whose simulated reflectivities best match the triple-frequency observations. The initial profile
is then generated using an onion-peeling approach that performs the database-matching process from the top downward, with
the retrieved attenuation at each step used to correct the measured reflectivity of the next layer (Liu and Mace, 2022; Liu
et al., 2022). During the radar OEM retrieval, the same CDF/EOF method and identical a priori constraints as those used in
380 the CoSSIR retrievals in Section 4.1 are applied. The IWC and D_{me} profiles retrieved from the triple-frequency radar are then
integrated to obtain the column-integrated IWP and D_m for the validation of the CoSSIR retrieval results.

4.3 Retrieval example

In this subsection, we select one representative cloud scene and present detailed retrieval results from CoSSIR observations
using the BMCI-only and hybrid BMCI-OEM approaches, along with retrievals from the triple-frequency radar observations for
385 a comprehensive comparison. The selected cloud scene occurs between 16:52 and 17:02 UTC on 15 January 2023. This flight
leg takes place during the tropical transition phase of an extra tropical storm, resulting in a particularly complex hydrometeor
vertical distribution. Figures 6-9 show the results obtained using the LargeBlockAggregate ice particle habit for both the
radiometer and radar retrievals.

Figure 6 shows the CoSSIR TB observations in blue for different channels, while the orange and green lines show the TB
390 simulations using retrievals from the BMCI and OEM, respectively. Again, the BMCI-only results are obtained by incremen-
tally inflating the measurement uncertainty until the required minimum of 25 database cases are identified. The OEM iteration
is initialized using the BMCI estimates, and these two lines evaluate the effectiveness of the OEM in reducing TB discrepan-
cies. It is evident that the TB agreement improves significantly after applying the OEM step. Using the BMCI-only results,
the simulations reproduce the observations of some channels reasonably well, but substantial negative biases remain, espe-
395 cially when the TBs have deep depressions around 16:57 UTC when the aircraft flew above thick clouds. Among the 183 GHz
channels, the 182.31 GHz channel shows the largest discrepancy, with agreement improving as the channel moves away from
the water vapor absorption line. A similar pattern is seen for the 325 GHz channels, where the ± 0.9 GHz channel exhibits the
largest mismatch, and the ± 11.5 GHz channel shows the best agreement. After applying the OEM, all channels except 325 ± 0.9
GHz show substantial improvement, with simulations closely reproducing the TB observations. Considering that the radiative
400 transfer model has many simplifications and assumptions, achieving such good agreement for both clear-sky and thick-cloud
scenes is impressive. The results also suggest that the BMCI-only approach may overestimate the overall cloud ice mass due
to the consistent cold biases in the simulated TBs relative to the observations.

The left-column panels in Figure 7 show the collocated W-, Ka-, and Ku-band radar reflectivity profiles, respectively, while
the right-column panels show the radar reflectivity residuals defined as reflectivity simulations minus observations for the W-,
405 Ka, and Ku-band retrievals. Overall, the simulated radar reflectivity profiles reproduce the observations reasonably well, with
most differences falling within ± 4 dBz. The W-band results show some negative biases within the frontal band. These biases
are expected partly due to the saturation of the W-band in very thick ice clouds, and partly as a compensation effect to minimize

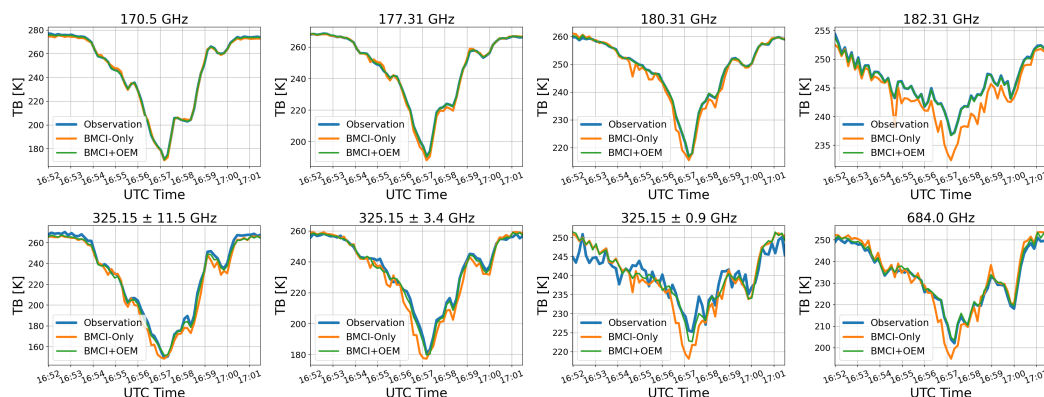


Figure 6. The blue lines show the CoSSIR brightness temperature (TB) observations for a representative cloud scene occurred on 15 January 2023 during the IMPACTS field campaign. The orange and green lines show the TB simulations computed from the BMCI-only and OEM retrieval results.

the cost function. For Ku band, biases are positive near echo top and become negative and largest above the melting band. As explained above, we do not perform LWC retrievals below the 273 K isotherm, nor do we aim to validate the algorithm for LWP retrievals, primarily due to the limitations of ARTS and other existing RTMs in accurately modeling radiative transfer within the melting layer.

Figure 8 shows the IWC and IWP retrievals from CoSSIR observations using the BMCI-only algorithm (left column) and hybrid BMCI-OEM algorithm (middle column), compared with the reference retrievals from triple-frequency radar observations (right column). Each column shows the retrieved IWC profiles at 240-meter vertical resolution (top), the corresponding IWC uncertainties (middle), and the IWP and associated uncertainty estimate (bottom). Compared to the radar retrievals that provide more detailed and smoothly varying cloud profiles, the radiometer retrievals generally capture the overall cloud structure, but finer internal details cannot be fully reproduced due to the limited information content in the TB observations. As the DoF shown in Figure 4 mostly ranges from 4 to 7, the radiometer observations have limited capability to constrain the vertical profiles, and a large portion of the constraints comes from the a priori information. For the BMCI-only retrievals, the most notable feature is the vertical extension beyond the expected cloud layers at both the cloud top and bottom. The internal cloud structure is also poorly characterized. Both sides of this flight leg (16:52-16:54 UTC and 17:00-17:01 UTC) contain almost no ice mass, but the BMCI-only algorithm indicates the presence of ice clouds. The OEM optimization shows the ability to moderately remove spurious cloud layers and to better highlight the internal structure. Although the OEM retrievals still show clouds on both sides of the curtain, these clouds are assigned to the correct altitudes with much thinner geometric thickness, making them more physically consistent with the radar reference for the anvil clouds. The uncertainty estimates from both algorithms show a similar pattern, with the cloud cores becoming more tightly constrained and the cloud top and bottom layers containing larger errors. Again, the hybrid BMCI-OEM method correctly retrieves the anvil cloud layer height on both sides, while the BMCI-only method does not. For the IWP retrievals shown in the bottom panels, the major IWP changes after apply-

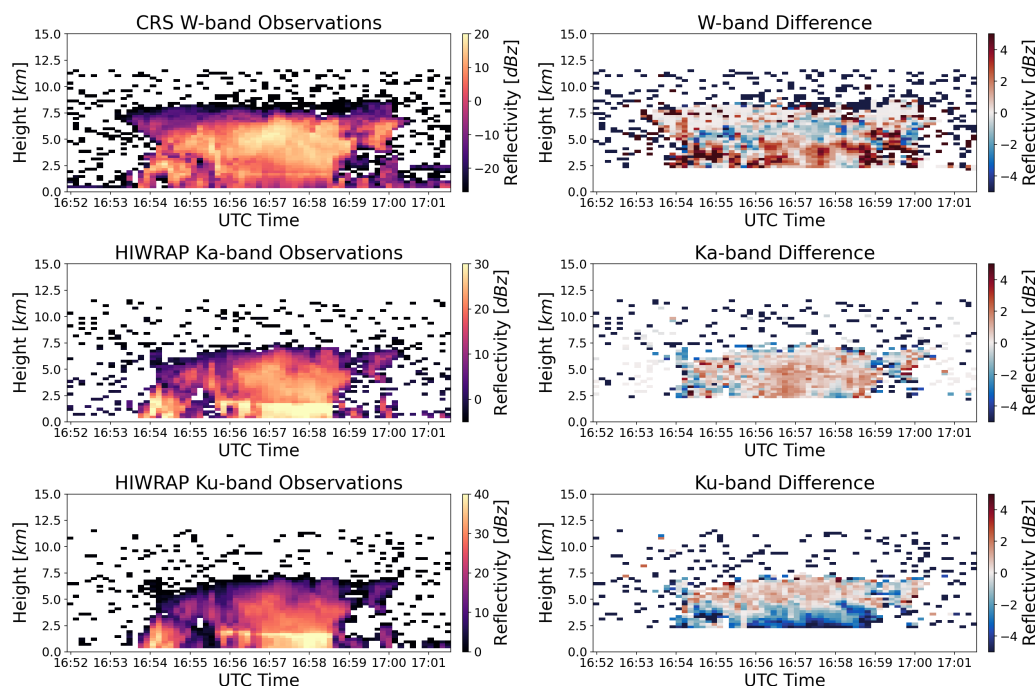


Figure 7. The left-column panels show the collocated W-, Ka-, and Ku-band radar reflectivity profiles corresponding to the same scene as the CoSSIR observations in Figure 6. The right-column panels present the radar reflectivity residuals that are defined as the simulated reflectivity minus the observations after applying the triple-frequency radar retrieval algorithm.

ing OEM occur around 16:57 UTC, coinciding with the largest TB depressions. While the BMCI-only retrievals show better agreement with the radar results during this period than the BMCI-OEM method, a more thorough comparison using a larger set of retrieval cases will be presented in Subsection 4.4. The radiometer-retrieved IWP and the radar retrievals show a similar trend, but notable differences are observed for the thick ice clouds in this selected retrieval example. For the radar retrievals, the uncertainty estimates for both IWC and IWP are small, reflecting the rich information content in the triple-frequency radar observations in constraining IWC.

Figure 9 shows the retrieval results for ice cloud particle size, and they are presented in the same format as Figure 8. As the calculation of D_{me} depends highly on the IWC due to the one-moment PSD assumption, the resulting particle size retrievals are similar to the IWC results in Figure 8. The radiometer retrieval results generally follow the radar-derived results, but they do not reproduce the detailed features in the D_{me} profiles. For the mean mass diameter D_m shown in the bottom panels, the retrieved values reach up to approximately 750 μm and are capped at this value. The limitation comes from both the maximum particle size in the SSD dataset and the specific PSD selected for the retrievals. Compared with the BMCI-only results, the OEM retrievals partially improve the positive biases on both sides of this cloud curtain. These large ice particles with very small IWC values are highly unlikely to exist in nature. In the future, we plan to develop customized criteria to filter out such

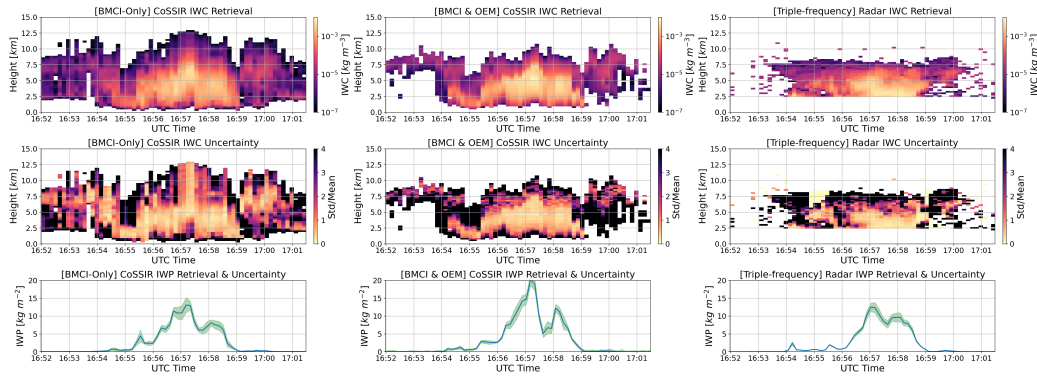


Figure 8. Ice water content (IWC) and ice water path (IWP) retrievals from CoSSIR observations using the BMCI-only algorithm (left column) and BMCI-OEM algorithm (middle column), with retrievals from the triple-frequency radar observations shown in the right column as the reference. Within each column, the retrieved IWC profiles, the corresponding IWC uncertainties in percentage, and the IWP along with its uncertainty estimate are presented, respectively.

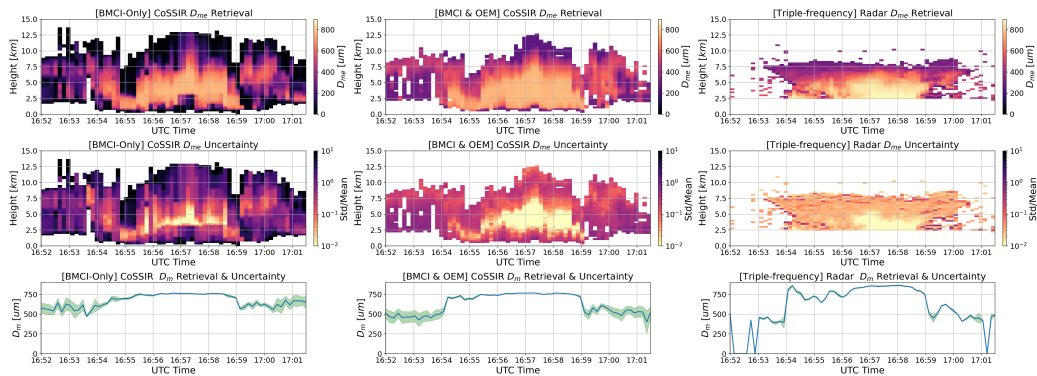


Figure 9. Same as Figure 8, but showing the vertical profiles of particle size D_{me} and the corresponding column-averaged mean mass diameter D_m .

spurious clouds or implement a cloud-flagging algorithm upfront to prevent such occurrences. One thing to note is that the BMCI-only retrievals are computed by directly applying BMCI to the D_m in the retrieval database, while the OEM retrievals are obtained by first computing the particle size D_{me} profiles and then performing the IWC-weighted calculations. For the radar retrievals, the detailed inner structure is well resolved, and the uncertainty estimates are small for both D_{me} profiles and the column-averaged D_m parameter.

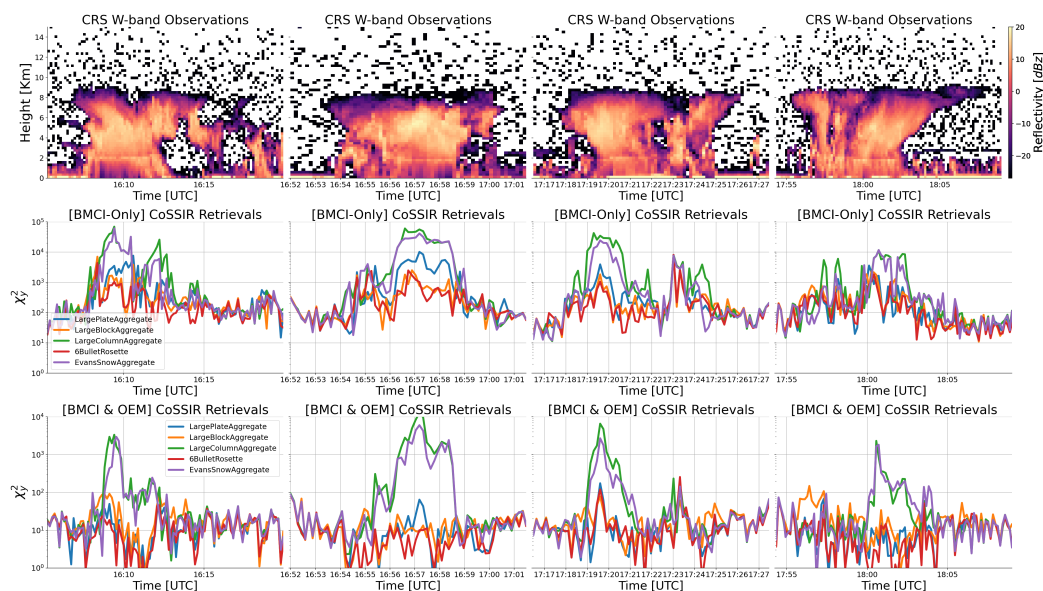


Figure 10. The top row shows the W-band CRS observations for four selected cloud scenes observed on 15 January 2023. The second row of panels shows the χ_y^2 values for the BMCI-only retrievals, and the third row presents the χ_y^2 values after applying the OEM. Results for five different ice cloud habits are presented.

4.4 Retrieval Statistics

In this subsection, we include additional CoSSIR observations and a broader set of ice cloud particle habits to provide a more comprehensive assessment of the radiometer retrievals relative to the collocated triple-frequency radar retrievals. Four deep cloud scenes on 15 January 2023 are selected, and five particle habits described in Section 2.2.2 are applied.

The top row of panels of Figure 10 shows the W-band CRS observations for the four selected cloud scenes observed on 15 January 2023. These observations were collected between roughly 16:00 and 18:30 UTC. The second row of panels shows the χ_y^2 values for the BMCI-only retrievals, and the third row shows the χ_y^2 values after applying the OEM. Results for all five different ice cloud habits are presented. The results further highlight the merits of OEM in reducing the TB discrepancies. For the BMCI-only retrievals, most χ_y^2 values fall within the range of 10^2 - 10^3 , except in the higher reflectivity cores of the clouds where the χ_y^2 values often exceed 10^3 . The results differ by particle habits, with the LargeColumnAggregate and EvansSnowAggregate habits in general showing higher χ_y^2 values than the other three habit assumptions. The improvements after applying the OEM are substantial. In general, the χ_y^2 values decrease by one to two orders of magnitude and fall below or close to the measurement uncertainties. Even in the dense ice cloud regions where the BMCI-only χ_y^2 values are extremely large, the OEM step reduces them to very small values. For the LargeColumnAggregate and EvansSnowAggregate, the χ_y^2 values do not reduce to comparable low levels, indicating the critical role of particle habit selection in determining retrieval performance.



Figure 11 compares the overall performance of CoSSIR and triple-frequency radar retrievals, with the first two columns
465 showing layer-level parameters (IWC and D_{me}) and the third and fourth columns showing column-integrated parameters
(IWP and mean mass diameter D_m), respectively. The BMCI-only and BMCI-OEM retrievals derived from CoSSIR are both
evaluated against the corresponding triple-frequency radar retrievals. The fifth column shows the median absolute logarithmic
error (MedALE) for each variable as a quantitative metric of retrieval accuracy. MedALE is defined as:

$$\text{MedALE} = \text{median} \left(\left| 10 \log_{10} \left(\frac{x_{\text{cossir}}}{x_{\text{radar}}} \right) \right| \right) \quad (8)$$

470 where x_{cossir} and x_{radar} denote the retrievals from the CoSSIR and triple-frequency radar observations, respectively. MedALE
is expressed in units of dB. Each row presents the results obtained using a different particle habit selection. It is seen that the
retrieval performance varies with particle habit selection. Among the five selected particle habits, the LargePlateAggregate,
LargeBlockAggregate and 6BulletRosette exhibit better constrained retrievals, while the LargeColumnAggregate and EvansS-
nowAggregate show poorer performance. Compared with the BMCI-only approach, the BMCI-OEM retrievals provide mod-
475 erate improvements for all four ice cloud variables. For the IWC retrievals shown in the first column, the OEM step moderately
reduces the positive biases present in the BMCI-only results and reduces the spread of the scatter. The IWC values retrieved
from radiometer observations generally follow the radar results, particularly for clouds with large IWC. This indicates that the
TB observations are sensitive to layer-resolved ice cloud microphysics. However, as the information content in the TB obser-
vations is limited, the radiometer retrievals still show a spread of nearly one order of magnitude relative to the radar results.
480 The MedALE for IWC ranges from 3.36 dB for the 6BulletRosette to 6.12 dB for the LargeColumnAggregate habit when
applying the hybrid BMCI-OEM algorithm. For the D_{me} profile retrievals, the BMCI results are widely scattered. The OEM
method reduces the divergence, but the retrieved particle sizes show persistent overestimation for $D_{me} < 700$ μm relative to the
triple-frequency radar retrievals. For the IWP retrievals shown in the third column, the OEM tends to consistently improve the
biases, and the scattered samples are generally better aligned with the diagonal. The MedALE for IWP shows evident decrease
485 after implementing OEM. For the LargePlateAggregate, LargeBlockAggregate, and 6BulletRosette habits, MedALE decreases
from the 3-4 dB range to the 2-3 dB range. Improvements in D_m retrievals are also apparent, as the OEM partially mitigates
the BMCI-only bias of overestimating low values and underestimating high values.

Finally, since the LargePlateAggregate, LargeBlockAggregate, and 6BulletRosette habits reproduce the TB observations
well (Figure 10), we average their MedALE values to quantify the retrieval accuracy. After applying the hybrid BMCI-OEM
490 algorithm, the differences between the CoSSIR-retrieved IWC, D_{me} , IWP, and D_m and the triple-frequency radar retrievals
are 3.75 dB, 0.82 dB, 2.53 dB, and 0.55 dB, respectively. The improvements of the hybrid BMCI-OEM algorithm over the
BMCI-only approach are 0.21 dB, 0.02 dB, 0.85 dB, and 0.13 dB for these four variables.

5 Summary and conclusions

This paper presents the hybrid BMCI-OEM retrieval algorithm that we developed for the submillimeter-wave radiometer in
495 support of the PolSIR and PMM missions. The primary retrieval products are IWP and mean mass diameter D_m , but the

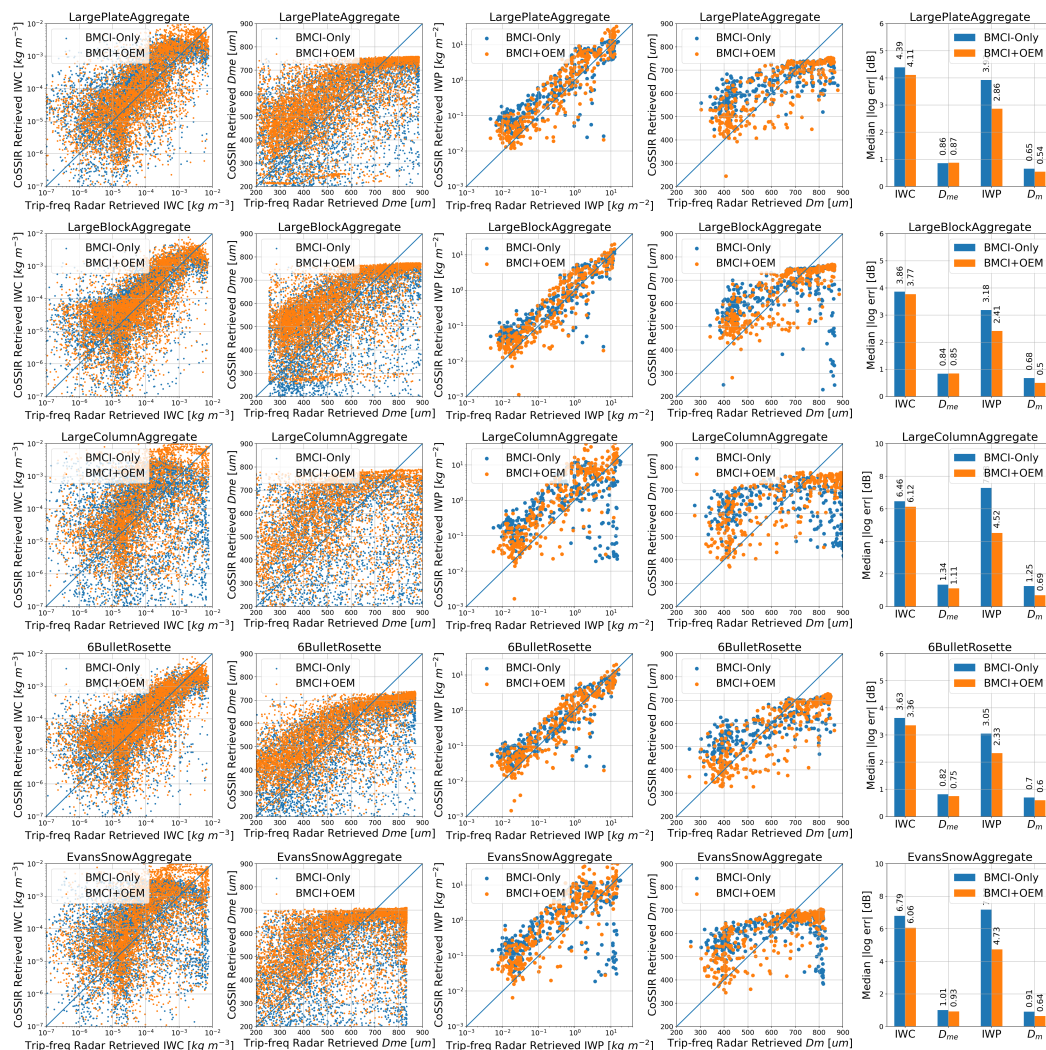


Figure 11. The scatterplots of the layer-level parameters including ice water content (IWC) and particle size in the first two columns, and the vertical integrated parameters including ice water path (IWP) and mean mass diameter (D_m) in the third and fourth columns. The BMCI-only and BMCI-OEM retrieval results from radiometer are compared with the triple-frequency radar retrievals. The fifth column shows the median absolute logarithmic error for each variable as a quantitative metric of retrieval accuracy. Each row corresponds to a different assumed ice cloud particle habit.

algorithm can also retrieve the vertical profile of ice and liquid cloud microphysical quantities and water vapor. The Bayesian algorithm employs a hybrid strategy that combines the advantage of BMCI and OEM. With a comprehensive a priori database, the computationally efficient BMCI method can handle most retrieval cases. For cases where the BMCI fails due to insufficient database cases matching the TB observations, the additional OEM approach is applied to further maximize the posterior PDF



500 and extend the retrieval capability beyond the limitations of the a priori database. With the CDF/EOF technique, the largely identical a priori constraints used in the BMCI step can be applied in the OEM step, even though the original a priori PDF in the retrieval database is highly non-Gaussian. The entire retrieval process therefore operates under reasonably consistent a priori constraints.

The hybrid BMCI-OEM algorithm is first applied to the evaluation of the C²OMODO radiometer using simulated observa-
505 tions. Retrieval results for IWP, LWP, IWV, and D_m are presented, and diagnostic analyses are performed based on the method provided by the OEM framework. Besides the column-integrated variables that are expected to become operational products for the PolSIR and PMM missions, we also explore potential vertical profiling capability using the averaging kernel matrix. The results indicate that the median vertical resolution achievable for ice cloud profiling is approximately 2.5 km. The DoF exhibits a positive dependence on IWP and IWV, and it typically ranges from 5 to 7 when the IWP exceeds 10 g m^{-2} . The
510 information content analysis indicates that higher IWP values correspond to higher information content. The 325 GHz channels contribute approximately 4 bits of additional information for IWP in the presence of the 183 GHz channels. Although the 89 GHz channel shows little benefit for IWP retrievals, it provides substantial information for the LWP and IWV retrievals.

The BMCI-only and hybrid BMCI-OEM algorithms are then applied to real CoSSIR observations collected during the IM-
515 PACTS campaign to further evaluate its performance. The ice cloud parameters retrieved from CoSSIR observations are compared against triple-frequency radar retrievals obtained from collocated observations from the CRS and HIWARP instruments, both of which are mounted on the same aircraft platform as CoSSIR. By upgrading the measurement vector and forward model, the hybrid BMCI-OEM algorithm is directly applied to the triple-frequency radar retrievals, highlighting the great extendibility of the hybrid Bayesian framework to other remote sensing measurements. The triple-frequency radar retrievals represent our best understanding of cloud profiles. Although we built a comprehensive database using all available CloudSat profiles within
520 a latitude-longitude domain, the BMCI-only results still exhibit significant TB discrepancies, especially when TB is significantly depressed by dense ice clouds. The OEM method is demonstrated to significantly improve the TB agreements, with simulations for almost all channels closely following the observations when certain particle habits are used. The simulation performance is sensitive to the selection of particle habit, as some particle habits fail to reproduce the observed TB. Compared to the triple-frequency radar retrievals, the vertical extent of the BMCI-retrieved profiles tends to exceed the expected cloud
525 layers at both cloud top and bottom, and the internal cloud structure is poorly resolved. The OEM method shows the ability to moderately remove spurious cloud layers and better highlight the cloud core. Statistical analysis indicates that the OEM provides moderate improvements over BMCI-only retrievals for both layer-resolved microphysical parameters and column-integrated variables. The OEM shows the advantage of reducing positive biases in the BMCI-only results and reducing errors. Also, the IWCs retrieved from radiometer observations generally follow the radar retrieved values, indicating the sensitivity of
530 TB observations to layer-level ice cloud microphysics. However, the limited information in TB leads to retrievals varying by nearly an order of magnitude around the radar results. Using MedALE as the evaluation metric, the CoSSIR-retrieved IWC, D_{me} , IWP, and D_m differ from the radar retrievals by 3.75 dB, 0.82 dB, 2.53 dB, and 0.55 dB, respectively, when applying the hybrid BMCI-OEM method. Compared with the BMCI-only retrievals, the errors are reduced by 0.21 dB, 0.02 dB, 0.85 dB, and 0.13 dB for these four variables.



535 In summary, compared to the BMCI-only algorithm, the additional OEM procedure significantly reduces TB discrepancies while keeping the a priori information largely consistent with that used in the BMCI step. Despite the significant improvements in TB agreements, enhancements in the retrieval accuracy of ice cloud microphysical quantities are moderate due to the limited information content in the TB observations. The posterior PDFs of the OEM retrievals are still largely constrained by the a priori information. The hybrid Bayesian framework also demonstrates its great extendibility to other remote sensing observations.

540 As more information becomes available through techniques such as multi-sensor integration or hyperspectral measurements, the hybrid Bayesian algorithmic framework shows increasing potential to better constrain cloud microphysics.

Data availability. The CloudSat data used to develop the a priori retrieval database are publicly available from the CloudSat Data Processing Center: <https://www.cloudsat.cira.colostate.edu/>. The CoSSIR and triple-frequency radar observations, along with the associated WRF dataset, are available through NASA's Earth science data collections: <https://www.earthdata.nasa.gov/data/projects/impacts/collection>.

545 *Author contributions.* YL, JG and IA developed the initial ideas together. YL and JG then designed the experiments. YL implemented the ideas, led the coding effort as well as the presentation of the current work. JG and IA provided guidance throughout this work and participated in the writing. RK provided the calibrated L1 CoSSIR observations. RC contributed to the development of the a priori database. RK, DW, RB and SB participated in discussions during the execution of this work and provided helpful suggestions.

Competing interests. The authors declare that no competing interests are present.

550 *Acknowledgements.* The authors acknowledge the CloudSat community for their work in generating and disseminating multi-level data products. They also acknowledge the IMPACTS team for executing the field campaign and publishing the resulting datasets. Finally, the authors extend their appreciation to the ARTS community for its sustained development of the radiative transfer model.

Financial support. This work was funded by NASA's PolSIR and PMM missions, as well as the NASA Earth Science Project Office (ESPO).



References

- 555 Adams, I., Kroodasma, R., Munchak, S., Fritts, M., and Milani, L.: The Configurable Scanning Submillimeter-wave Instrument/Radiometer (CoSSIR): Modernizing Submillimeter Radiometry for Future Cloud Investigations, in: AGU Fall Meeting, pp. A197–10, AGU, 2020.
- Aires, F., Prigent, C., Bernardo, F., Jiménez, C., Saunders, R., and Brunel, P.: A Tool to Estimate Land-Surface Emissivities at Microwave frequencies (TELSEM) for use in numerical weather prediction, *Quarterly Journal of the Royal Meteorological Society*, 137, 690–699, 2011.
- 560 Auguste, F. and Chaboureau, J.: Deep convection as inferred from the C2OMODO concept of a tandem of microwave radiometers, *Frontiers in Remote Sensing*, 3, 852 610, 2022.
- Austin, R., Heymsfield, A., and Stephens, G.: Retrieval of ice cloud microphysical parameters using the CloudSat millimeter-wave radar and temperature, *Journal of Geophysical Research: Atmospheres*, 114, 2009.
- Brath, M., Fox, S., Eriksson, P., Harlow, R., Burgdorf, M., and Buehler, S.: Retrieval of an ice water path over the ocean from ISMAR and
565 MARSS millimeter and submillimeter brightness temperatures, *Atmospheric Measurement Techniques*, 11, 611–632, 2018.
- Brogniez, H., Roca, R., Auguste, F., Chaboureau, J., Haddad, Z., Munchak, S., Li, X., Bouniol, D., Depee, A., Fiolleau, T., and Kollias, P.: Time-delayed tandem microwave observations of tropical deep convection: Overview of the C2OMODO mission, *Frontiers in Remote Sensing*, 3, 854 735, 2022.
- Buehler, S., Jiménez, C., Evans, K., Eriksson, P., Rydberg, B., Heymsfield, A., Stubenrauch, C., Lohmann, U., Emde, C., John, V., and
570 Sreerakha, T.: A concept for a satellite mission to measure cloud ice water path, ice particle size, and cloud altitude, *Quarterly Journal of the Royal Meteorological Society: A journal of the atmospheric sciences, applied meteorology and physical oceanography*, 133, 109–128, 2007.
- Buehler, S., Defer, E., Evans, F., Eliasson, S., Mendrok, J., Eriksson, P., Lee, C., Jiménez, C., Prigent, C., Crewell, S., and Kasai, Y.: Observing ice clouds in the submillimeter spectral range: the CloudIce mission proposal for ESA’s Earth Explorer 8, *Atmospheric Measurement
575 Techniques Discussions*, 5, 1101–1151, 2012.
- Buehler, S., Mendrok, J., Eriksson, P., Perrin, A., Larsson, R., and Lemke, O.: ARTS, the atmospheric radiative transfer simulator–version 2.2, *Geoscientific Model Development*, 11, 1537–1556, 2018.
- Deng, M., Mace, G., Wang, Z., and Berry, E.: CloudSat 2C-ICE product update with a new Ze parameterization in lidar-only region, *Journal of Geophysical Research: Atmospheres*, 120, 12–198, 2015.
- 580 Eriksson, P., Ekelund, R., Mendrok, J., Brath, M., Lemke, O., and Buehler, S.: A general database of hydrometeor single scattering properties at microwave and sub-millimetre wavelengths, *Earth System Science Data*, 10, 1301–1326, 2018.
- Eriksson, P., Rydberg, B., Mattioli, V., Thoss, A., Accadia, C., Klein, U., and Buehler, S.: Towards an operational Ice Cloud Imager (ICI) retrieval product, *Atmospheric Measurement Techniques*, 13, 53–71, 2020.
- Eriksson, P., Emrich, A., Kempe, K., Riesbeck, J., Aljarosha, A., Auriacombe, O., Kugelberg, J., Hekma, E., Albers, R., Murk, A., and
585 Møller Pedersen, S.: The Arctic Weather Satellite radiometer, *Atmospheric Measurement Techniques*, 18, 4709–4729, 2025.
- Evans, K., Wang, J., O’C Starr, D., Heymsfield, G., Li, L., Tian, L., Lawson, R., Heymsfield, A., and Bansemmer, A.: Ice hydrometeor profile retrieval algorithm for high-frequency microwave radiometers: application to the CoSSIR instrument during TC4, *Atmospheric Measurement Techniques*, 5, 2277–2306, 2012.
- Evans, K. F., Walter, S. J., Heymsfield, A. J., and McFarquhar, G. M.: Submillimeter-wave cloud ice radiometer: Simulations of retrieval
590 algorithm performance, *Journal of Geophysical Research*, 107, 2002.



- Evans, K. F., Wang, J. R., Racette, P. E., Heymsfield, G., and Li, L.: Ice cloud retrievals and analysis with the compact scanning submillimeter imaging radiometer and the cloud radar system during CRYSTAL FACE, *Journal of Applied Meteorology*, p. 839–859, 2005.
- Field, P., Heymsfield, A., and Bansemer, A.: Snow size distribution parameterization for midlatitude and tropical ice clouds, *Journal of the Atmospheric Sciences*, 64, 4346–4365, 2007.
- 595 Fox, S., Lee, C., Moyna, B., Philipp, M., Rule, I., Rogers, S., King, R., Oldfield, M., Rea, S., Henry, M., and Wang, H.: ISMAR: an airborne submillimetre radiometer, *Atmospheric Measurement Techniques*, 10, 477–490, 2017.
- Gong, J., Wu, D., and Eriksson, P.: The first global 883 GHz cloud ice survey: IceCube Level 1 data calibration, processing and analysis, *Earth System Science Data*, 13, 5369–5387, 2021.
- Iki, K., Takayama, S., Nio, T., Okada, K., and Furukawa, K.: Overview of precipitation measuring mission (PMM): the next generation rain
600 mission, *Remote Sensing of the Atmosphere, Clouds, and Precipitation VIII*, 13262, 76–80, 2025.
- Kummerow, C., Ringerud, S., Crook, J., Randel, D., and Berg, W.: An observationally generated a priori database for microwave rainfall retrievals, *Journal of Atmospheric and Oceanic Technology*, 28, 113–130, 2011.
- Li, L., Heymsfield, G., Carswell, J., Schaubert, D., McLinden, M., Creticos, J., Perrine, M., Coon, M., Cervantes, J., Vega, M., and Guimond, S.: The NASA high-altitude imaging wind and rain airborne profiler, *IEEE Transactions on Geoscience and Remote Sensing*, 54, 298–310,
605 2015.
- Liu, Y. and Adams, I.: Tomographic reconstruction algorithms for retrieving two-dimensional ice cloud microphysical parameters using along-track (sub) millimeter-wave radiometer observations, *Atmospheric Measurement Techniques*, 18, 1659–1674, 2025.
- Liu, Y. and Mace, G.: Assessing synergistic radar and radiometer capability in retrieving ice cloud microphysics based on hybrid Bayesian algorithms, *Atmospheric Measurement Techniques*, 15, 927–944, 2022.
- 610 Liu, Y., Buehler, S. A., Brath, M., Liu, H., and Dong, X.: Ensemble Optimization Retrieval Algorithm of Hydrometeor Profiles for the Ice Cloud Imager Submillimeter-Wave Radiometer, *Journal of Geophysical Research: Atmospheres*, 123, 4594–4612, 2018.
- Liu, Y., Mace, G., and Posselt, D.: Assessing synergistic radar and radiometer retrievals of ice cloud microphysics for the Atmosphere Observing System (AOS) architecture, *IEEE Transactions on Geoscience and Remote Sensing*, 60, 1–14, 2022.
- Mathur, A., Gangwar, R., Gohil, B., Deb, S., Kumar, P., Shukla, M., Simon, B., and Pal, P.: Humidity profile retrieval from SAPHIR on-board
615 the Megha-Tropiques, *Current Science*, 104, 1650–1655, 2013.
- May, E. and Eriksson, P.: The Ice Cloud Imager: retrieval of frozen water mass profiles, *EGUsphere*, 18, 7243–7266, 2025.
- May, E., Rydberg, B., Kaur, I., Mattioli, V., Hallborn, H., and Eriksson, P.: The Ice Cloud Imager: retrieval of frozen water column properties, *Atmospheric Measurement Techniques*, 17, 5957–5987, 2024.
- McLinden, W., M.L., Li, L., Heymsfield, G., Coon, M., and Emory, A.: The NASA GSFC 94-GHz airborne solid-state cloud radar system
620 (CRS), *Journal of Atmospheric and Oceanic Technology*, 38, 1001–1017, 2021.
- McMurdie, L., Heymsfield, G., Yorks, J., Braun, S., Skofronick-Jackson, G., Rauber, R., Yuter, S., Colle, B., McFarquhar, G., Poellot, M., and Novak, D.: Chasing snowstorms: The Investigation of Microphysics and Precipitation for Atlantic coast-threatening snowstorms (IMPACTS) campaign, *Bulletin of the American Meteorological Society*, 103, E1243–E1269, 2022.
- Pfreundschuh, S., Eriksson, P., Duncan, D., Rydberg, B., Håkansson, N., and Thoss, A.: A neural network approach to estimating a posteriori
625 distributions of Bayesian retrieval problems, *Atmospheric Measurement Techniques*, 11, 4627–4643, 2018.
- Pfreundschuh, S., Eriksson, P., Buehler, S., Brath, M., Duncan, D., Larsson, R., and Ekelund, R.: Synergistic radar and radiometer retrievals of ice hydrometeors, *Atmospheric Measurement Techniques*, 13, 4219–4245, 2020.



- Prigent, C., Aires, F., Wang, D., Fox, S., and Harlow, C.: Sea-surface emissivity parametrization from microwaves to millimetre waves, *Quarterly Journal of the Royal Meteorological Society*, 143, 596–605, 2017.
- 630 Rodgers, C. D.: *Inverse methods for atmospheric sounding: theory and practice*, vol. 2, World scientific, 2000.
- Stamnes, K., Tsay, S., Wiscombe, W., and Jayaweera, K.: Numerically stable algorithm for discrete-ordinate-method radiative transfer in multiple scattering and emitting layered media, *Applied optics*, 27, 2502–2509, 1988.
- Wu, D., Gong, J., Deal, W., Gaines, W., Cooke, C., De Amici, G., Pantina, P., Liu, Y., Yang, P., Eriksson, P., and Bennartz, R.: Remote sensing of ice cloud properties with millimeter and submillimeter-wave polarimetry, *IEEE Journal of Microwaves*, 4, 847–857, 2024.
- 635 Yorks, J., Miller, M., Lang, T., Finlon, J., Adams, I., Colle, B., Greybush, S., Heymsfield, A., Heymsfield, G., Kroodsma, R., and LeBlanc, S.: Sampling Strategies to Optimize Coincident Remote Sensing and In Situ Cloud and Precipitation Observations from Multiple Aircraft, *Bulletin of the American Meteorological Society*, 106, E2544–E2562, 2025.